One-step solid state reaction to selectively fabricate cubic and tetragonal CuFe$_2$O$_4$ anode material for high power lithium ion batteries

Zheng Xing[a], Zhicheng Ju[a,*], Jian Yang[b,**], Huayun Xu[b], Yitai Qian[a,b]

[a] Hefei National Laboratory for Physical Sciences at Microscale and Department of Chemistry, University of Science and Technology of China, Hefei, Anhui 230026, PR China
[b] School of Chemistry and Chemical Engineering, Shandong University, Jinan 250100, PR China

ARTICLE INFO

ABSTRACT

Cubic CuFe$_2$O$_4$ (c-CuFe$_2$O$_4$) and tetragonal CuFe$_2$O$_4$ (t-CuFe$_2$O$_4$) nanoparticles were selectively prepared using a facile one-step solid state reaction route by ferrous oxalate and copper acetate as the reactants. As an anode material for Li-ion batteries, compared with c-CuFe$_2$O$_4$ and t-CuFe$_2$O$_4$ synthesized at 800 °C, c-CuFe$_2$O$_4$ synthesized at 400 °C with smaller particle size and larger surface area exhibited superior discharge capacities and better cycling performance (950 mAh g^{-1} at 100 mA g^{-1} after 60 cycles), and higher rate capability. The influence of the two crystal phases on the electrochemical performance were only exhibited at the Li$^+$ insertion process during the first discharge. The average particle size and the surface areas play an important role in effecting the lithium-ion storage capability and cycling ability. Through *ex situ* HRTEM analysis, we observed the existence of metastable Fe$_x$Cu$_{1-x}$ alloy in the discharged nanocomposition for the first time, which exhibits the interaction of metallic Cu particles with the adjacent iron ions.

1. Introduction

Spinel ferrites MFe$_2$O$_4$ (M = Mn, Mg, Zn, Ni, Co, *etc.*) and their related structures have been extensively researched, due to their theoretical configurations and magnetic properties [1–4]. In recent years, the spinel ferrites MFe$_2$O$_4$ with high lithium-ion storage capability has been reported, because they can effectively improve the electrochemical properties of simple iron oxides [5,6]. By adjusting the chemical identity of M^{2+}, the crystal structure of MFe$_2$O$_4$ can be molecularly engineered to tune the energy density and working voltages and provide high specific capacity, good cycling stability and excellent rate performance [7]. A variety of spinel ferrites have been synthesized to applied as anode materials for lithium-ion battery (LIB), including NiFe$_2$O$_4$ [8], CoFe$_2$O$_4$ [9,10], ZnFe$_2$O$_4$ [11,12], MgFe$_2$O$_4$ [13], and CdFe$_2$O$_4$ [14].

Copper ferrite (CuFe$_2$O$_4$) has also been investigated as an anode materials for LIB, due to its low toxicity, large abundance and high theoretical specific capacity than graphite. The crystal structure of CuFe$_2$O$_4$ can be described as Cu^{2+} and Fe^{3+} ions occupied tetrahedral (A-) and octahedral (B-) crystallographic sites formed by cubic close-packed arrangement of O^{2-} ions. The cation distribution in the two sites caused different symmetries of CuFe$_2$O$_4$. So the copper ferrites not only have normal cubic phase, but also possess tetragonal unit-cell symmetry [15,16]. The transformation process of the two phases were carefully researched by Prabhu et al. through a remarkable *in situ* high temperature XRD method [17].

Both cubic and tetragonal phase of CuFe$_2$O$_4$ were employed as the anode on LIB. T-CuFe$_2$O$_4$ thin film synthesized by electrodeposition and further anodization of CuFe$_2$ alloys was first applied as LIB electrode; the initial reversible capacity was 452 mAh g^{-1} at a current density of 10 μA cm^{-2} and 75% of the capacity was kept over 100 cycles [18]. Ultra-fine powders of t-CuFe$_2$O$_4$/SnO$_2$ nanocomposites prepared by a urea-nitrate combustion method provided a first discharge capacity of 849 mAh g^{-1} [19]. The t-CuFe$_2$O$_4$ prepared by the thermal decomposition of a metal citrate precursor at 800 °C delivered the capacity of nearly 500 mAh g^{-1} after 50 cycles [20]. Carbon coated hollow nanospheres of c-CuFe$_2$O$_4$ synthesized through polymer-templated hydrothermal growth method and subsequent calcination maintained a specific capacity of 550 mAh g^{-1} even after the 70th cycles at the current density of 60 mA g^{-1} [21]. Cu–Fe–O oxide system based on t-CuFe$_2$O$_4$ with a variation of Cu and Fe from 4:1 to 1:4 prepared by a two step self-combustion method confirms that the presence of copper improve the stability of the iron oxide electrode

* Corresponding author. Tel.: +86 5513601589.
** Corresponding author.
E-mail addresses: juzc@ustc.edu.cn (Z. Ju), yangjian@sdu.edu.cn (J. Yang).

[22]. However, the effect of composition and structure to the electrochemical performances as anode in LIB was not widely investigated so far.

In this paper, we report a facile one-step solid state reaction method to selectively synthesize c-CuFe$_2$O$_4$ and t-CuFe$_2$O$_4$ submicron-particles, using ferrous oxalate and copper acetate as the reactants. The crystal structure, morphology and surface area of CuFe$_2$O$_4$ are researched by XRD, TEM, HRTEM and N$_2$ adsorption. The electrochemical properties of the two different phases are characterized and compared in terms of cyclic voltammetry and discharge/charge profiles. The c-CuFe$_2$O$_4$ synthesized at 400 °C with particle size of 50–100 nm exhibits high capacity of 950 mAh g^{-1} at 100 mA g^{-1} after 60 cycles; in contrast, both c-CuFe$_2$O$_4$ and t-CuFe$_2$O$_4$ with larger particle sizes deliver lower specific capacity during the galvanostatic cycling tests. The involved electrode reactions during the discharge/charge processes of c-CuFe$_2$O$_4$ are investigated based on the *ex situ* HRTEM analysis. We observed the existence of metastable Fe$_x$Cu$_{1-x}$ alloy in the discharged nanocomposition for the first time, which might explain the interaction of metallic Cu particles with the adjacent iron ions to enhance the stability of the electrode.

2. Experimental

All reagents (purchased from Sinopharm Chemical Reagent Co., Ltd.) were analytically pure and used without further purification.

2.1. Synthesis of cubic and tetragonal CuFe$_2$O$_4$

The nano-sized c-CuFe$_2$O$_4$ was synthesized by a facile thermal oxidation process. In a typical procedure, ferrous oxalate dihydrate (FeC$_2$O$_4$·2H$_2$O) and copper acetate (Cu(CH$_3$COO)$_2$·H$_2$O) with the stoichiometric ratio of 2:1 were mixed and ball milled (QM-3SP2 Planetary Ball Mill produced by Nanjing University Instrument plant) for 5 h at speed of 400 rpm. Then, the mixture was calcined at 400 °C for 6 h in a tube-furnace in continuous argon flow and the c-CuFe$_2$O$_4$ (400 °C) was obtained. If the mixture was calcined at 800 °C for 6 h in N$_2$ flow, the c-CuFe$_2$O$_4$ (800 °C) was fabricated instead. Moreover, if the mixture was calcined at 800 °C for 6 h and the atmosphere was changed into the air, the t-CuFe$_2$O$_4$ was synthesized.

2.2. Sample characterization

The phase of the sample was recorded by X-ray powder diffraction (XRD) on a Bruker AXS D8 Advance X-ray diffractometer equipped with Cu Ka radiation ($\lambda = 1.54182$ Å). The nanostructures were characterized using transmission electron microscope (TEM, JEM 1011 microscope operated at 100 kV), selected area electron diffraction (SAED) pattern and high-resolution transmission electron microscope (HRTEM, JEOL-2010 and JEOL-2100 operated at 200 kV). The surface areas of the sample were performed through measuring N$_2$ adsorption–desorption isotherms by TriStar II 3020 (Micromeritics Instrument Corporation, U.S.A.).

2.3. Electrochemical measurements

The active material (60 wt%), Super P acetylene black (30 wt%) and polyvinylidene fluoride (PVDF) (10 wt%) dissolved in N-methyl pyrrolidone (NMP) were mixed and ball milled for 5 h at speed of 400 rpm to prepare the uniform slurry. Then the slurry was coated on a copper current collector and dried at 80 °C under vacuum for 12 h. Li metal was applied as counter electrode. The Celgard 2300 microporous membrane was used as polypropylene separator, and LiPF$_6$ (1 M) solution dissolved in ethylene carbonate (EC)/dimethyl carbonate (DMC) by 1:1 volume ratio was used
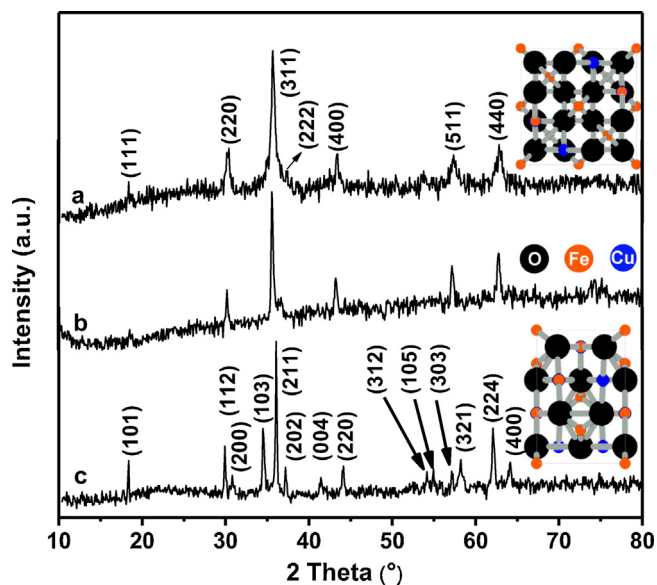

Fig. 1. The typical XRD patterns of the as-prepared CuFe$_2$O$_4$ samples: (a) c-CuFe$_2$O$_4$ synthesized at 400 °C; (b) c-CuFe$_2$O$_4$ synthesized at 800 °C; (c) t-CuFe$_2$O$_4$.

as the electrolyte. The coin-type cells (size: 2032) were assembled in the argon filled glove box (Mikrouna, Super 1220/750/900). The galvanostatic charge–discharge tests in the potential range of 0.01–3.00 V (*vs.* Li+/Li) were performed on LAND-CT2001A battery cycler at room temperature. The cyclic voltammetry (CV) profiles were tested at a scanning rate of 0.1 mV s^{-1} by LK-2005A electrochemical workstation (Lanlike, Tianjin China).

3. Result and discussion

Fig. 1 shows the typical XRD patterns of as-prepared product. All the reflection peaks in Fig. 1a could be indexed as CuFe$_2$O$_4$ with face-centered cubic phase (JCPDS Card Files, no. 77-0010, $Fd3m$). The lattice constant calculated from the pattern is 8.343 Å, very close to the reported data ($a = 8.370$ Å). The broadened diffraction peaks and low intensity indicate that low crystallinity. As shown in the inset of Fig. 1a, c-CuFe$_2$O$_4$ possesses a normal spinel structure with all the Cu^{2+} cations on the tetrahedral (A-) sites and the Fe^{3+} cations on the octahedral (B-) site occupying the fcc lattice composed by close-packed O^{2-} anions. The peaks of XRD pattern of c-CuFe$_2$O$_4$ (800 °C) shown Fig. 1b was the same as c-CuFe$_2$O$_4$ (400 °C), which is also consistent with the JCPDS card 77-0010. The broadening peaks become a little narrower as the temperature turns higher especially the reflection of (2 2 2) crystal surface. The presence of impurities was negligible, including Fe$_3$O$_4$, Fe$_2$O$_3$, and CuO.

The XRD pattern in Fig. 1c is determined to be body-centered tetragonal CuFe$_2$O$_4$. The unit cell parameters are calculated to be $a = 5.796$ Å and $c = 8.710$ Å, which are compatible with the reported value (JCPDS Card Files, no. 34-0425, $a = 5.844$ Å, $c = 8.630$ Å, space group $I4_1/amd$). No significant amounts of impurities were observed. The structure of t-CuFe$_2$O$_4$ is shown in the inset of Fig. 1c an inverse spinel structure in which Cu^{2+} cations mainly occupied B-sites, and Fe^{3+} cations are on B-sites and A-sites with approximately equal occupancy.

The particle morphology and crystal structure of the as-prepared samples were investigated by TEM and HRTEM analysis. Fig. 2a indicates that the c-CuFe$_2$O$_4$ (400 °C) is composed of nano particles with size of 50–100 nm. The HRTEM image in Fig. 2b shows a representative nano particle of c-CuFe$_2$O$_4$ (400 °C). The interlayer distances of the two vertical planes are calculated to be 4.85Å and
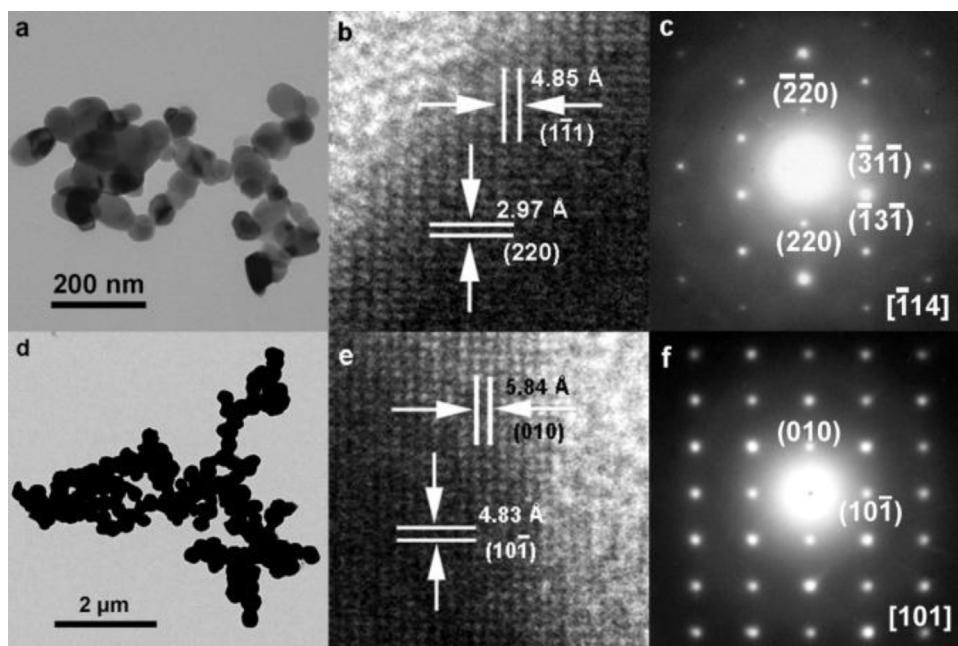
Fig. 2. (a) Representative TEM image of c-CuFe$_2$O$_4$ (400 °C); (b) HRTEM image of c-CuFe$_2$O$_4$ (400 °C); (c) SAED pattern from [$\bar{1}$ 1 4] direction; (d) TEM image of t-CuFe$_2$O$_4$; (e) HRTEM image of the t-CuFe$_2$O$_4$; (f) corresponding SAED pattern.

2.97Å, which could be ascribed to the (1 1 1) and (2 2 0) planes of c-CuFe$_2$O$_4$, respectively. The selected area electron diffraction (SAED) in Fig. 2c is determined to be taken from [$\bar{1}$ 1 4] zone axis. In addition, the average particle size of c-CuFe$_2$O$_4$ (800 °C) were about 500–800 nm which is clearly shown in SFig. 1 (Support Information). The crystallite size was much larger than c-CuFe$_2$O$_4$ (400 °C) which could be caused by the higher sintering temperature [20].

The TEM image in Fig. 2d shows that t-CuFe$_2$O$_4$ consists of nanoparticles with average crystallite size of 400–600 nm. A typical HRTEM image taken on a t-CuFe$_2$O$_4$ particle is shown in Fig. 2e. The fringe spacings are evaluated to be about 5.84 Å and 4.83 Å, corresponding to those of the (0 1 0) and (1 0 $\bar{1}$) planes of t-CuFe$_2$O$_4$, respectively. The corresponding SAED pattern in Fig. 2f comprises diffraction point which could be assigned to the vertical (0 1 0) and (1 0 $\bar{1}$) planes of t-CuFe$_2$O$_4$.

The Brunauer–Emmett–Teller (BET) method with N$_2$ adsorption was applied to investigate the specific surface area data of the as-prepared samples. The BET surface area data of c-CuFe$_2$O$_4$ (400 °C), c-CuFe$_2$O$_4$ (800 °C) and t-CuFe$_2$O$_4$ were calculated to be about 18.94 m^2 g^{-1}, 0.59 m^2 g^{-1} and 1.35 m^2 g^{-1}, respectively, without noticeable microporosity nor mesoporosity, which is in accordance with the TEM images. The decrease of surface areas from c-CuFe$_2$O$_4$ (400 °C) to c-CuFe$_2$O$_4$ (800 °C) and t-CuFe$_2$O$_4$ could be related to the increase of sintering temperature which could promote particle size growth [23].

The electrochemical behavior of the two phases was also been thoroughly researched. The cyclic voltammetry (CV) test was taken at scan rate of 0.1 mV s^{-1} in the voltage range of 0.01–3.0 V vs Li$^+$/Li, and the CV profiles of first ten cycles are shown in Fig. 3. According to Fig. 3a, in the first discharge cycle, the c-CuFe$_2$O$_4$ (400 °C) shows a small peak at 0.85 V which could be assigned to the formation of stable intermediate Li$_n$CuFe$_2$O$_4$ [21]. The following cathodic peak at 0.55 V could be ascribed to electrochemical reduction with Li into Cu^0 and Fe^0, and the formation of Li$_2$O. In the first charge process, two anodic peaks located at 1.69 V and 1.83 V could be attributed to the stepwise oxidation of Fe^0/Fe^{3+} and Cu^0/Cu^{2+}, respectively. During the successive cycles, only one cathodic peak at 0.89 V is observed which is higher than Fe^{3+}/Fe^0 (0.7 V) [24] and lower than
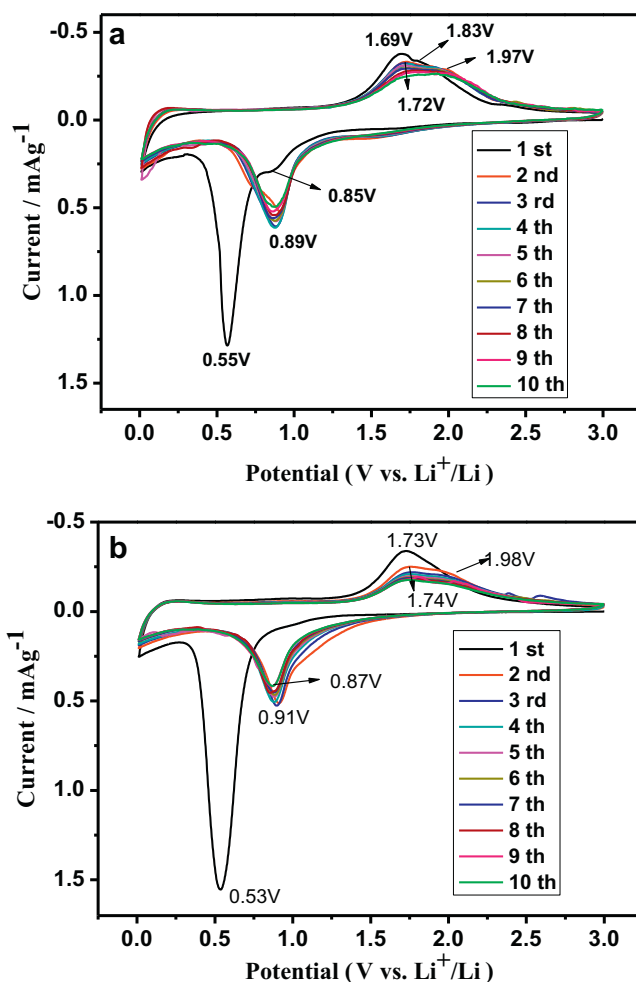

Fig. 3. Cyclic voltammograms profiles of the c-CuFe$_2$O$_4$ (400 °C) (a), and t-CuFe$_2$O$_4$ (b) electrode with 0.1 mV s^{-1} (0.01–3.0 V vs Li$^+$/Li, 10 cycles).
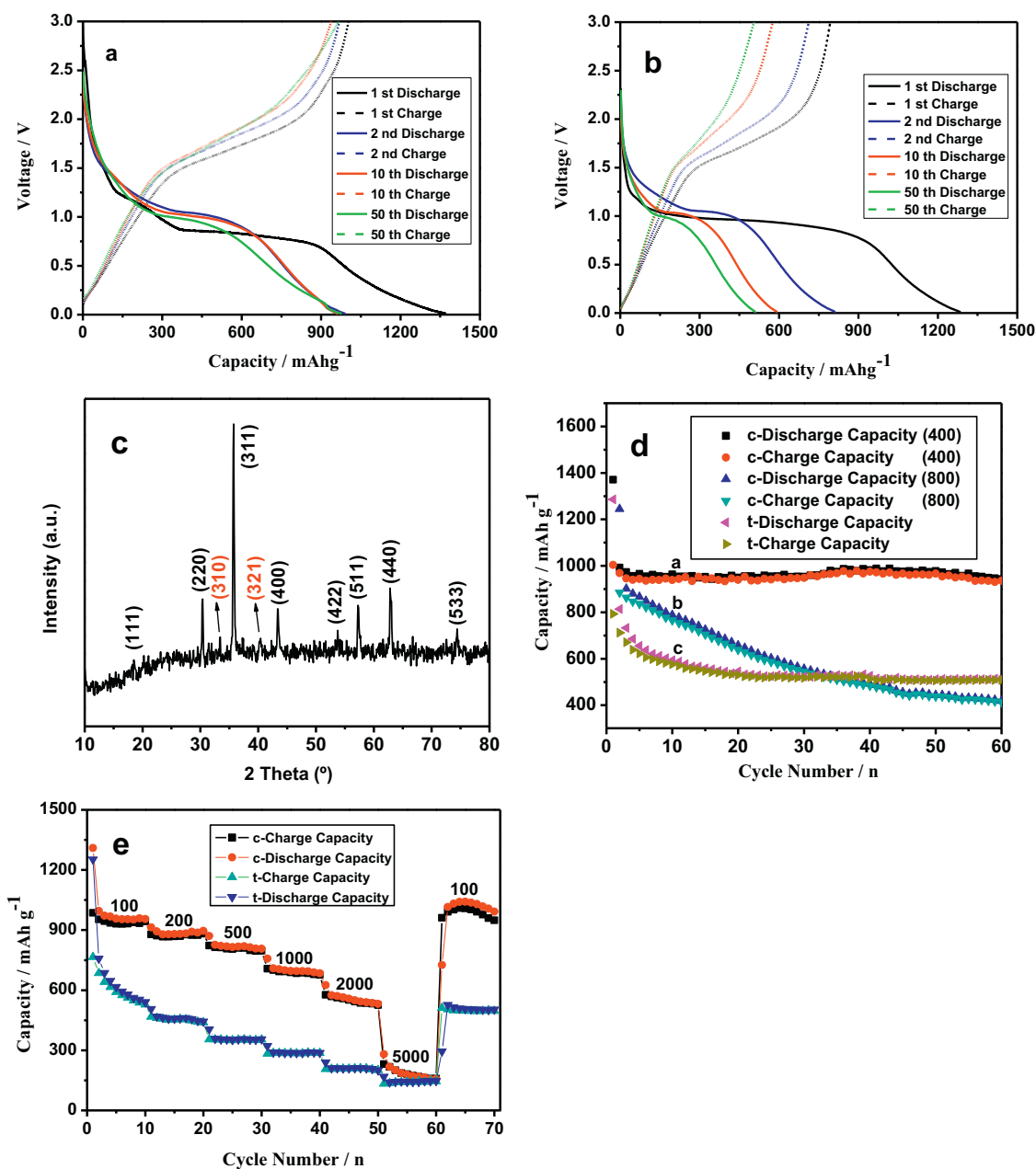
Fig. 4. Electrochemical performance of the $CuFe_2O_4$ electrode: (a) discharge/charge profiles for selected cycles of c-$CuFe_2O_4$ (400 °C); (b) discharge/charge profiles for selected cycles of t-$CuFe_2O_4$; (c) *ex situ* XRD pattern of c-$CuFe_2O_4$ (400 °C) electrode after discharged to 1.1 V; (d) discharge/charge capacity of c-$CuFe_2O_4$ (400 °C), c-$CuFe_2O_4$ (800 °C) and t-$CuFe_2O_4$ as a function of cycle number; (e) rate performance of c-$CuFe_2O_4$ (400 °C) and t-$CuFe_2O_4$ electrode (100–5000 mA g^{-1}).

Cu^{2+}/Cu^{+} (1.2 V) [25], that might because individual reduction processes of Fe^{3+} and Cu^{2+} emerged into one peak [7]. The subsequent anodic peaks are analogous to the first scan but only slightly shifted to 1.72 V and 1.97 V. The positively shift between first and the subsequent cycles should be corresponding to the polarization of the electrode [26]. Moreover, the intensity and position of the peaks after the first cycle steadily maintains which indicates that the discharge/charge process is stable.

Compared with c-$CuFe_2O_4$, t-$CuFe_2O_4$ shows one cathodic peak (0.53 V) and one anodic peak (1.73 V) during the first cycle (Fig. 3b). Then the first oxidation procedure of Fe^0/Fe^{3+} and Cu^0/Cu^{2+} was amalgamated into one peak. The successive discharge/charge profiles were similar as the c-$CuFe_2O_4$, which implies that the electrode reactions of t-$CuFe_2O_4$ could be the same as c-$CuFe_2O_4$. The peak at 0.85 V of c-$CuFe_2O_4$ in the first discharge process is the only one distinct phenomenon, which indicates that the intermediate

$Li_nCuFe_2O_4$ did not formed during the first discharge of t-$CuFe_2O_4$ [20].

Galvanostatic cycling tests of the samples were examined at a current density of 100 mA g^{-1} between 0.01 V and 3.00 V with Li foil as a counter electrode at room temperature (25 °C). The first discharge curve of c-$CuFe_2O_4$ (400 °C) (Fig. 4a) shows a smooth voltage decrease to 1.2 V in the first place, then a short plateau-like step at about 1.1 V, followed by a second voltage drop ending at 0.85 V. According to the previous report, the preceding intercalation process corresponds to the reaction of $CuFe_2O_4 + nLi \rightarrow Li_nCuFe_2O_4$ [21]. In order to get structural information of the Li insertion phase, *ex situ* XRD measurement was performed after the electrode was discharged to 1.1 V. As shown in Fig. 4c, the c-$CuFe_2O_4$ reflection did not show visible shift, while the small peaks at 33.7° and 40.4° were emerged which implies that the lithium insertion reduced the symmetry of unit cell. The two peaks could be assigned to (2 2 1) and

(3 1 0) crystal surfaces of the primitive cubic structure. This suggests that an insertion phase such as $Li_nCuFe_2O_4$ may be formed during discharge. Reflections due to Li_2O and metal Cu and Fe are barely discernible.

The following voltage plateau at 0.85 V could be attributed to the reactions of $Cu^{2+} \rightarrow Cu^0$ and $Fe^{3+} \rightarrow Fe^0$ [27,28]. Then a sloping curve after the conversion could be explained as the electrolyte decomposition and interfacial storage [29]. These reactions provide a capacity about 1370 mAh g^{-1} (equivalent to ~12.2 mol Li per mol c-$CuFe_2O_4$ (400 °C)). The first charge slope shows a reversible charge capacity of about 1003 mAh g^{-1} (~8.9 mol Li per mol c-$CuFe_2O_4$ (400 °C)), corresponding to the oxidation of Cu^0 and Fe^0. After the first cycle, the discharge and charge reversible capacities are stable at about 950 mAh g^{-1} and 930 mAh g^{-1}, respectively. Moreover, the first discharge/charge curves of c-$CuFe_2O_4$ (800 °C) (SFig. 2, SI) are similar as c-$CuFe_2O_4$ (400 °C) while the capacity is much lower.

Fig. 4b shows discharge/charge profiles of t-$CuFe_2O_4$. Compared with that in Fig. 4a, both discharge curves show a long voltage plateau below 1.0 V; the only distinct phenomenon is that the short plateau-like step at 1.1 V is not observed during the first discharge which is consistent with the CV test. According to the report of Lavela's group, stable intermediate phase $Li_nCuFe_2O_4$ was not formed when Li$^+$ intercalated into the t-$CuFe_2O_4$ crystal framework [20], and the t-$CuFe_2O_4$ is directly reduced to Fe^0 and Cu^0. The initial discharge and charge specific capacities are about 1286 mAh g^{-1} and 793 mAh g^{-1}, which are lower than c-$CuFe_2O_4$. Moreover, the discharge and charge capacities severely fade after the first cycle.

The cycling performances of the c-$CuFe_2O_4$ (400 °C), c-$CuFe_2O_4$ (800 °C) and t-$CuFe_2O_4$ at 100 mA g^{-1} are presented in Fig. 4d. After the second cycle, the discharge capacity of c-$CuFe_2O_4$ (400 °C) is stable at ~950 mAh g^{-1} (8.48 mol Li) after 60 cycles with little capacity fading, demonstrating superior capacity retention capability. The columbic efficiency of c-$CuFe_2O_4$ (400 °C) is about 73% in the first cycle, and all above 97% in the subsequent cycles. In contrast, the c-$CuFe_2O_4$ (800 °C) delivers an initial specific capacity of 1240 mAh g^{-1} (11.07 mol Li) and then gradually fades to 420 mAh g^{-1} over 60 cycles with a columbic efficiency of 71% in the first cycle, and all above 96% after that. Moreover, the reversible specific capacity of t-$CuFe_2O_4$ decays significantly in the first ten cycles and finally maintains at above 510 mAh g^{-1} (4.55 mol Li) until 60 cycles. The columbic efficiency of t-$CuFe_2O_4$ is 62% in the first cycle and then gradually increases and stays at 97% after 10 cycles.
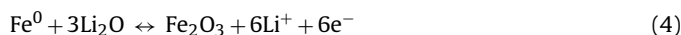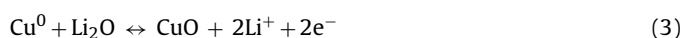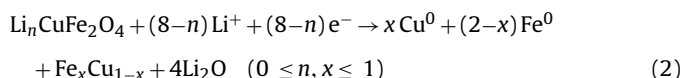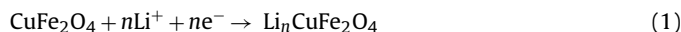
Besides the discharge/charge cycling, the rate performances of the two phases were also tested at the current densities of 100, 200, 500, 1000, 2000, and 5000 mA g^{-1}. The average capacities of c-$CuFe_2O_4$ (400 °C) were 960, 880, 810, 690, 540 and 150 mAh g^{-1}, respectively. The capacity severely decayed when the current increased to 5000 mA g^{-1}. The rate capacity of t-$CuFe_2O_4$ was also lower than c-$CuFe_2O_4$ (400 °C); however, when the current raised up to 5000 mA g^{-1}, the specific capacity was almost the same as c-$CuFe_2O_4$ (400 °C) (140 mAh g^{-1}). After rate test at high rates, the specific capacity of both phase was recovered and possessed an increasing amount at 100 mA g^{-1}, which implies that the structure of the electrodes are stable during the high current. The high capacities observed at high rates suggest that c-$CuFe_2O_4$ (400 °C) could be a potential anode material for power LIBs.

Base on the discussion above, during the first discharge, the t-$CuFe_2O_4$ crystal structure accommodates less lithium ion and the Li$^+$ intercalation process is shorter than the c-$CuFe_2O_4$ before the structure deformed. However, although the initial structure of the two different phases are distinct, when the strong changes occurring during the first discharge, similar electrode composition was formed and induced similar performances as active materials in lithium cells. Because smaller particle size with larger surface

area lead to higher electrode/electrolyte contact area and better charge/discharge rates, which not only be favorable for fast kinetic property to facilitate the electron transportation and the Li$^+$ transportation but also decrease volume expansion during cycling [30,31]. So the particle sizes have a strong influence on the specific capacity and cycling stability. In this case, the higher Li$^+$ storage capacities and rate retention capability of c-$CuFe_2O_4$ (400 °C) than t-$CuFe_2O_4$ and c-$CuFe_2O_4$ (800 °C) could be attributed to the decrease of the particle size and increase of the surface areas.

According to CV and galvanostatic cycling tests, the two phases of $CuFe_2O_4$ exhibited similar electrode reactions during the first cycle. So we took c-$CuFe_2O_4$ (400 °C) as an example for ex situ HRTEM analysis; the samples are carried out on the totally discharged (0.01 V) and fully charged (3.00 V) electrode materials after 50 cycles to identify the lithiation and delithiation induced structural reorganization of electrode materials. Close inspection of the HRTEM image in Fig. 5a shows that when c-$CuFe_2O_4$ (400 °C) is fully reduced by lithium, the long-range ordering crystal structure completely disintegrated, and the particles are composed of nanocrystallites (5–8 nm) dispersed in an amorphous matrix, indicating significant structural changes. According to the previous research, the amorphous phase is Li_2O and the crystalline region are metal nanoparticles [32]. However, we observed an interesting phenomenon that there are several groups of lattice fringes which do not match any interplanar distances or superlattice distances of metal Cu and Fe. However, these lattice distances are consistent with a metastable phase formation of Fe_xCu_{1-x} with cubic structure (JCPDS 49-1399), for example, 2.46 Å could be indexed as the (2 2 2) crystal surface [33]. Furthermore, as marked in the square, there is an edge dislocation existed in the Fe_xCu_{1-x} alloy composition. The HRTEM of the fully recharged electrode material was shown in Fig. 5b; the pseudo-amorphous characters of the crystal structure are retained. As deduced from the lattice fringes, the nanocrystallites changed into Fe_2O_3 and CuO separately instead of c-$CuFe_2O_4$.

It could be inferred from the HRTEM images that during the first discharge, lithium-driven structural reorganization takes place and the initial material is reduced to nanocrystalline Cu, Fe and randomly dispersed in amorphous Li_2O matrix. In this case, the result of the electrochemical conversion of with Li is the formation of Li_2O/Cu/Fe nanocomposites with a large contact interface between different components. The Cu and Fe nanocrystals are not only aggregated separately, but also form metastable alloys. This existing state demonstrates the interaction of metallic Cu in situ form with the neighborhood of iron ions which could stabilize oxidation/reduction behavior of $CuFe_2O_4$ electrode under galvanostatic cycling conditions to avoid degradation [22]. The succeeding reversible process involves the formation and decomposition of Li_2O, accompanying the reduction/oxidation of Fe_2O_3/CuO nanoparticles (in the range 5–8 nm) respectively. The electrode with nanosized and pseudo-amorphous characters is maintained on the following discharge/charge processes.

$$CuFe_2O_4 + nLi^+ + ne^- \rightarrow Li_nCuFe_2O_4 \tag{1}$$

$$Li_nCuFe_2O_4 + (8-n)Li^+ + (8-n)e^- \rightarrow xCu^0 + (2-x)Fe^0$$
$$+ Fe_xCu_{1-x} + 4Li_2O \quad (0 \le n, x \le 1) \tag{2}$$

$$Cu^0 + Li_2O \leftrightarrow CuO + 2Li^+ + 2e^- \tag{3}$$

$$Fe^0 + 3Li_2O \leftrightarrow Fe_2O_3 + 6Li^+ + 6e^- \tag{4}$$

According to the previous research [21] and the experiment results, the possible electrode reactions of c-$CuFe_2O_4$ are proposed.
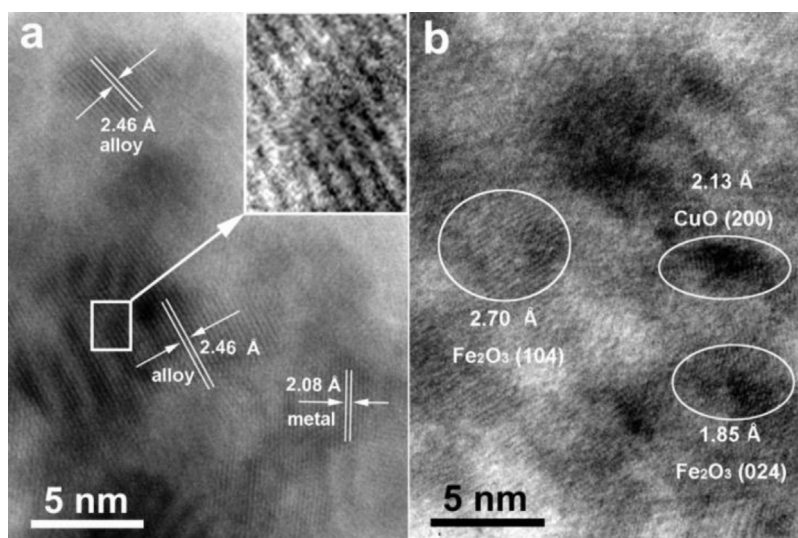
Fig. 5. (a) _Ex situ_ HRTEM image of metastable phase formation of Fe_xCu_{1-x} and metal particles in a typical c-$CuFe_2O_4$ (400 °C) electrode material after fully discharged (the inset in the corner shows an edge dislocation in the alloy); (b) _ex situ_ HRTEM after totally recharged.

As present in Eq. (1), during the first step of discharge, the preceding lithium intercalation occurres and intermediate phase $Li_nCuFe_2O_4$ arises (It is worth mentioning that this intermediate phase is hardly observed in the t-$CuFe_2O_4$ [34].). Then Li^+ ions involves conversion reaction occurred, the crystal structure deforms to the nano composition of Cu/Fe metal and Fe_xCu_{1-x} alloy dispersed in amorphous Li_2O (Eq. (2)). Both Eqs. (1) and (2) are irreversible and only carried out in the first discharge. During the charge process (Eqs. (3) and (4)) both metal nanoparticles can be reversibly oxidized by Li_2O through the conversion reaction forming the respective metal oxides [35].

4. Conclusion

In summary, we successfully developed a simple one-step solid state reaction route to selectively fabricate $CuFe_2O_4$ with different phase and size as a high-performance anode material for LIB. The c-$CuFe_2O_4$ (400 °C) electrode exhibits high capacity retention of 950 mAh g^{-1} after the 60th cycles at a current density of 100 mA g^{-1}, on the other hand, c-$CuFe_2O_4$ (800 °C) and t-$CuFe_2O_4$ with larger particle size and smaller specific surface area deliver lower capacities and charge/discharge rates. The only distinction of the electrode behavior between the different crystal phases are appeared at the lithium intercalation procedure during the first discharge. After lithium-driven structural reorganization, both electrode reactions are changed to the similar oxidation/reduction process of Fe^0/Fe^{3+} and Cu^0/Cu^{2+}. The decrease in the particle size and increase of the surface area was the main reason for an increase of the Li^+ storage sites or capacities from c-$CuFe_2O_4$ and t-$CuFe_2O_4$. Moreover, a Fe_xCu_{1-x} alloy was observed for the first time in the nano composition after discharge which illustrates the interaction of part of metallic Cu _in situ_ formed with the conterminous Fe ions.

Acknowledgements

Appendix A. Supplementary data

Supplementary data associated with this article can be found, in the online version, at http://dx.doi.org/10.1016/j.electacta.2013.03.174.

References

[1] U. Jeong, X. Teng, Y. Wang, H. Yang, Y. Xia, Superparamagnetic colloids: controlled synthesis and Niche applications, Advanced Materials 19 (2007) 33.
[2] S. Sun, H. Zeng, D.B. Robinson, S. Raoux, P.M. Rice, S.X. Wang, G. Li, Monodisperse MFe$_2$O$_4$ (M = Fe, Co, Mn) nanoparticles, Journal of the American Chemical Society 126 (2003) 273.
[3] Y. Xu, D.S. Xue, D.Q. Gao, J.L. Fu, X.L. Fan, D.W. Guo, B. Gao, W.B. Sui, Ordered CoFe$_2$O$_4$ nanowire arrays with preferred crystal orientation and magnetic anisotropy, Electrochimica Acta 54 (2009) 5684.
[4] J. Fu, J. Zhang, Y. Peng, J. Zhao, G. Tan, N.J. Mellors, E. Xie, W. Han, Unique magnetic properties and magnetization reversal process of CoFe$_2$O$_4$ nanotubes fabricated by electrospinning, Nanoscale 4 (2012) 3932.
[5] Y.-N. NuLi, Y.-Q. Chu, Q.-Z. Qin, Nanocrystalline ZnFe$_2$O$_4$ and Ag-doped ZnFe$_2$O$_4$ films used as new anode materials for Li-ion batteries, Journal of the Electrochemical Society 151 (2004) A1077.
[6] M. Li, Y.-X. Yin, C. Li, F. Zhang, L.-J. Wan, S. Xu, D.G. Evans, Well-dispersed bi-component-active CoO/CoFe$_2$O$_4$ nanocomposites with tunable performances as anode materials for lithium-ion batteries, Chemical Communications 48 (2012) 410.
[7] J. Cabana, L. Monconduit, D. Larcher, M.R. Palacín, Beyond intercalation-based Li-ion batteries: the state of the art and challenges of electrode materials reacting through conversion reactions, Advanced Materials 22 (2010) E170.
[8] P. Lavela, J.L. Tirado, CoFe$_2$O$_4$ and NiFe$_2$O$_4$ synthesized by sol–gel procedures for their use as anode materials for Li ion batteries, Journal of Power Sources 172 (2007) 379.
[9] Z.H. Li, T.P. Zhao, X.Y. Zhan, D.S. Gao, Q.Z. Xiao, G.T. Lei, High capacity three-dimensional ordered macroporous CoFe$_2$O$_4$ as anode material for lithium ion batteries, Electrochimica Acta 55 (2010) 4594.
[10] H. Xia, D. Zhu, Y. Fu, X. Wang, CoFe$_2$O$_4$-graphene nanocomposite as a high-capacity anode material for lithium-ion batteries, Electrochimica Acta 83 (2012) 166.
[11] Y. Sharma, N. Sharma, G. Rao, B. Chowdari, Li-storage and cyclability of urea combustion derived ZnFe$_2$O$_4$ as anode for Li-ion batteries, Electrochimica Acta 53 (2008) 2380.
[12] Z. Xing, Z. Ju, J. Yang, H. Xu, Y. Qian, One-step hydrothermal synthesis of ZnFe$_2$O$_4$ nano-octahedrons as a high capacity anode material for Li-ion batteries, Nano Research 5 (2012) 477.
[13] C. Gong, Y.-J. Bai, Y.-X. Qi, N. Lun, J. Feng, Preparation of carbon-coated MgFe$_2$O$_4$ with excellent cycling and rate performance, Electrochimica Acta 90 (2013) 119.
[14] Y. Sharma, N. Sharma, G.V.S. Rao, B.V.R. Chowdari, Li-storage and cycling properties of spinel, CdFe$_2$O$_4$, as an anode for lithium ion batteries, Bulletin of Materials Science 32 (2009) 295.
[15] J.Z. Jiang, G.F. Goya, H.R. Rechenberg, Magnetic properties of nanostructured CuFe$_2$O$_4$, Journal of Physics-Condensed Matter 11 (1999) 4063.

[16] G.F. Goya, H.R. Rechenberg, J.Z. Jiang, Magnetic irreversibility and relaxation in $CuFe_2O_4$ nanoparticles, Journal of Magnetism and Magnetic Materials 218 (2000) 221.

[17] D. Prabhu, A. Narayanasamy, K. Shinoda, B. Jeyadeven, J.M. Greneche, K. Chattopadhyay, Grain size effect on the phase transformation temperature of nanostructured $CuFe_2O_4$, Journal of Applied Physics 109 (2011) 013532.

[18] Y.-N. NuLi, Q.-Z. Qin, Nanocrystalline transition metal ferrite thin films prepared by an electrochemical route for Li-ion batteries, Journal of Power Sources 142 (2005) 292.

[19] R. Kalai Selvan, N. Kalaiselvi, C.O. Augustin, C.H. Doh, C. Sanjeeviraja, $CuFe_2O_4/SnO_2$ nanocomposites as anodes for Li-ion batteries, Journal of Power Sources 157 (2006) 522.

[20] M. Bomio, P. Lavela, J.L. Tirado, ^{57}Fe Mössbauer spectroscopy and electron microscopy study of metal extraction from $CuFe_2O_4$ electrodes in lithium cells, ChemPhysChem 8 (2007) 1999.

[21] L. Jin, Y. Qiu, H. Deng, W. Li, H. Li, S. Yang, Hollow $CuFe_2O_4$ spheres encapsulated in carbon shells as an anode material for rechargeable lithium-ion batteries, Electrochimica Acta 56 (2011) 9127.

[22] W. Gruner, J. Thomas, L. Giebeler, H. Ehrenberg, D. Wadewitz, Interactions of copper and iron in conversion reactions of nanosized oxides with large variations in iron–copper ratio, Journal of the Electrochemical Society 158 (2011) A1383.

[23] M. Mouallem-Bahout, S. Bertrand, O. Peña, Synthesis and characterization of $Zn_{1-x}Ni_xFe_2O_4$ spinels prepared by a citrate precursor, Journal of Solid State Chemistry 178 (2005) 1080.

[24] B. Wang, J.S. Chen, H.B. Wu, Z. Wang, X.W. Lou, Quasiemulsion-templated formation of alpha-Fe_2O_3 hollow spheres with enhanced lithium storage properties, Journal of the American Chemical Society 133 (2011) 17146.

[25] X.H. Huang, C.B. Wang, S.Y. Zhang, F. Zhou, CuO/C microspheres as anode materials for lithium ion batteries, Electrochimica Acta 56 (2011) 6752.

[26] J.Z. Wang, C. Zhong, D. Wexler, N.H. Idris, Z.X. Wang, L.Q. Chen, H.K. Liu, Graphene-encapsulated Fe_3O_4 nanoparticles with 3D laminated structure as superior anode in lithium ion batteries, Chemistry 17 (2011) 661.

[27] D. Larcher, C. Masquelier, D. Bonnin, Y. Chabre, V. Masson, J.-B. Leriche, J.-M. Tarascon, Effect of particle size on lithium intercalation into α-Fe_2O_3, Journal of the Electrochemical Society 150 (2003) A133.

[28] N. Yamakawa, M. Jiang, C.P. Grey, Investigation of the conversion reaction mechanisms for binary Copper(II) compounds by solid-state NMR spectroscopy and X-ray diffraction, Chemistry of Materials 21 (2009) 3162.

[29] S. Grugeon, S. Laruelle, L. Dupont, J.M. Tarascon, An update on the reactivity of nanoparticles Co-based compounds towards Li, Solid State Sciences 5 (2003) 895.

[30] A.S. Arico, P. Bruce, B. Scrosati, J.M. Tarascon, W. Van Schalkwijk, Nanostructured materials for advanced energy conversion and storage devices, Nature Materials 4 (2005) 366.

[31] P.G. Bruce, B. Scrosati, J.M. Tarascon, Nanomaterials for rechargeable lithium batteries, Angewandte Chemie International Edition in English 47 (2008) 2930.

[32] P. Poizot, S. Laruelle, S. Grugeon, L. Dupont, J.M. Tarascon, Nano-sized transition-metal oxides as negative-electrode materials for lithium-ion batteries, Nature 407 (2000) 496.

[33] F. Pan, T. Yang, K. Tao, B.X. Liu, Metastable phase formation in the Fe–Cu system by ion irradiation and solid state interdiffusion, Physica Status Solidi (a) 135 (1993) 199.

[34] M. Bomio, P. Lavela, J.L. Tirado, Electrochemical evaluation of $CuFe_2O_4$ samples obtained by sol–gel methods used as anodes in lithium batteries, Journal of Solid State Electrochemistry 12 (2007) 729.

[35] X. Zhu, Y. Zhu, S. Murali, M.D. Stoller, R.S. Ruoff, Nanostructured reduced graphene oxide/Fe_2O_3 composite as a high-performance anode material for lithium ion batteries, ACS Nano 5 (2011) 3333.